LETTER

doi:10.1038/nature12187

Cloning of Dirac fermions in graphene superlattices

L. A. Ponomarenko[1], R. V. Gorbachev[2], G. L. Yu[1], D. C. Elias[1], R. Jalil[2], A. A. Patel[3], A. Mishchenko[1], A. S. Mayorov[1], C. R. Woods[1], J. R. Wallbank[3], M. Mucha-Kruczynski[3], B. A. Piot[4], M. Potemski[4], I. V. Grigorieva[1], K. S. Novoselov[1], F. Guinea[5], V. I. Fal'ko[3] & A. K. Geim[1,2]

Superlattices have attracted great interest because their use may make it possible to modify the spectra of two-dimensional electron systems and, ultimately, create materials with tailored electronic properties[1–8]. In previous studies (see, for example, refs 1–8), it proved difficult to realize superlattices with short periodicities and weak disorder, and most of their observed features could be explained in terms of cyclotron orbits commensurate with the superlattice[1–4]. Evidence for the formation of superlattice minibands (forming a fractal spectrum known as Hofstadter's butterfly[9]) has been limited to the observation of new low-field oscillations[5] and an internal structure within Landau levels[6–8]. Here we report transport properties of graphene placed on a boron nitride substrate and accurately aligned along its crystallographic directions. The substrate's moiré potential[10–12] acts as a superlattice and leads to profound changes in the graphene's electronic spectrum. Second-generation Dirac points[13–22] appear as pronounced peaks in resistivity, accompanied by reversal of the Hall effect. The latter indicates that the effective sign of the charge carriers changes within graphene's conduction and valence bands. Strong magnetic fields lead to Zak-type cloning[23] of the third generation of Dirac points, which are observed as numerous neutrality points in fields where a unit fraction of the flux quantum pierces the superlattice unit cell. Graphene superlattices such as this one provide a way of studying the rich physics expected in incommensurable quantum systems[7–9,22–24] and illustrate the possibility of controllably modifying the electronic spectra of two-dimensional atomic crystals by varying their crystallographic alignment within van der Waals heterostuctures[25].

Since the first observation of Weiss oscillations[1,2], two-dimensional electronic systems subjected to a periodic potential have been studied in great detail[3–8]. The advent of graphene rapidly sparked interest in graphene superlattices[13–22]. The principal novelty of such superlattices is the Dirac-like spectrum and the fact that charge carriers are not buried deep under the surface, which allows a relatively strong superlattice potential on the nanometre scale. One promising method of making nanoscale graphene superlattices is the use of a potential induced by another crystal. For example, graphene placed on top of graphite or hexagonal boron nitride (hBN) exhibits a moiré pattern[10–12,26], and the graphene's tunnelling density of states becomes strongly modified[12,26], indicating the formation of superlattice minibands. This spectral reconstruction occurs near the edges of the superlattice Brillouin zone (SBZ) that are characterized[12,22] by wavevector $G = 4\pi/\sqrt{3}D$ and energy $E_S = \hbar v_F G/2$ (D is the superlattice period, v_F is graphene's Fermi velocity and $\hbar$ is Planck's constant divided by 2π).

To observe moiré minibands in transport properties, graphene has to be doped so that the Fermi energy reaches the reconstructed part of the spectrum. This imposes severe constraints on the misalignment angle, θ, of the graphene relative to the hBN substrate. Indeed, D is determined from θ and the 1.8% difference between the two lattice constants[12]. In the case of perfect alignment ($\theta = 0$), D has a maximum value of $\sim 13 \pm 1$ nm (ref. 12), which yields $E_S \approx 0.2$ eV. This energy scale corresponds to a carrier density of $n \approx 3 \times 10^{12}$ cm^{-2}, which is achievable by field-effect doping. However, misorientation by only 2° decreases D by a factor of two[12], and fourfold greater values of n are necessary for the Fermi energy to reach the edges of the first SBZ. In practice, studies of the superlattice spectrum in monolayer graphene require $\theta \leq 1^\circ$ (Methods).

Here we study high-mobility encapsulated graphene devices that are similar to those reported previously[27] but which involve a new element: crystallographic alignment between the graphene and the hBN with a precision of $\sim 1^\circ$. Figure 1 shows typical behaviour of longitudinal and Hall resistivities (ρ_{xx} and ρ_{xy}, respectively) for our aligned devices. There is the standard peak in ρ_{xx} at $n = 0$, graphene's main neutrality point. In addition, two other peaks appear symmetrically, one on either side of the main neutrality point, at high doping, $n = \pm n_S$. At low temperatures (T), the secondary peak on the hole side is stronger than that at the main neutrality point, whereas that on the electron side is ~ 10 times weaker. The reversal in sign of ρ_{xy} (Fig. 1b) cannot be explained by additional scattering and proves that hole-like and electron-like carriers appear in the conduction and, respectively, valence bands of graphene. We attribute the extra neutrality points to the superlattice potential induced by the hBN, which results in minibands featuring isolated secondary Dirac points (Fig. 1a, inset). This interpretation agrees with theory[12–22] and the tunnelling features reported in ref. 12, including the fact that those were stronger in the valence band.

Near the main neutrality point, the aligned devices have transport characteristics typical for graphene on hBN[27,28]. The conductivity $\sigma(n) = 1/\rho_{xx}$ varies linearly with n and can therefore be described in terms of constant mobility, μ. For the reported devices, we find that $\mu \approx (20\text{–}80) \times 10^3$ cm^2 V^{-1} s^{-1} for $|n| > 10^{11}$ cm^{-2}. Around the secondary neutrality points, σ depends linearly on $n - n_S$. At the hole-side secondary neutrality point (hSNP), at low temperature μ is practically the same as at the main neutrality point, whereas near the electron-side secondary neutrality point we find even higher values, $\mu \approx (30\text{–}100) \times 10^3$ cm^2 V^{-1} s^{-1}. However, at the main and secondary neutrality points the T dependences of both μ and the minimum conductivities are very different. This is discussed in Supplementary Information, section 1, and here we note only that the observed functions $\sigma(T)$ do not support the idea of major energy gaps being induced by the superlattice at the cloned secondary Dirac points[19–22] (Fig. 1a, inset). Furthermore, following the approach described in ref. 29, we analysed the thermal broadening of the peaks in ρ_{xx} (Supplementary Information, section 2). The analysis proves that the spectrum at the secondary neutrality points is linear, that is, Dirac-like, in agreement with theory[13–22].

Figure 2 shows the evolution of $\rho_{xx}(n)$ with increasing perpendicular magnetic field, B. Near the main Dirac point, we observe the standard[30] quantum Hall effect (QHE) for graphene, with plateaux in ρ_{xy} and zeros in ρ_{xx} at filling factors $\nu \equiv n\phi_0/B = \pm 2, \pm 6, \pm 10, \ldots$ where ϕ_0 is the flux quantum. Fan diagrams around the secondary Dirac points are different (Fig. 2). The resistance peak of the hSNP first broadens with increasing B and then splits into two maxima. The maxima correspond

[1]School of Physics and Astronomy, University of Manchester, Manchester M13 9PL, UK. [2]Centre for Mesoscience and Nanotechnology, University of Manchester, Manchester M13 9PL, UK. [3]Physics Department, Lancaster University, Lancaster LA1 4YB, UK. [4]Laboratoire National des Champs Magnétiques Intenses, CNRS-UJF-UPS-INSA, F-38042 Grenoble, France. [5]Instituto de Ciencia de Materiales de Madrid, Sor Juana Inés de la Cruz 3, Madrid 28049, Spain.

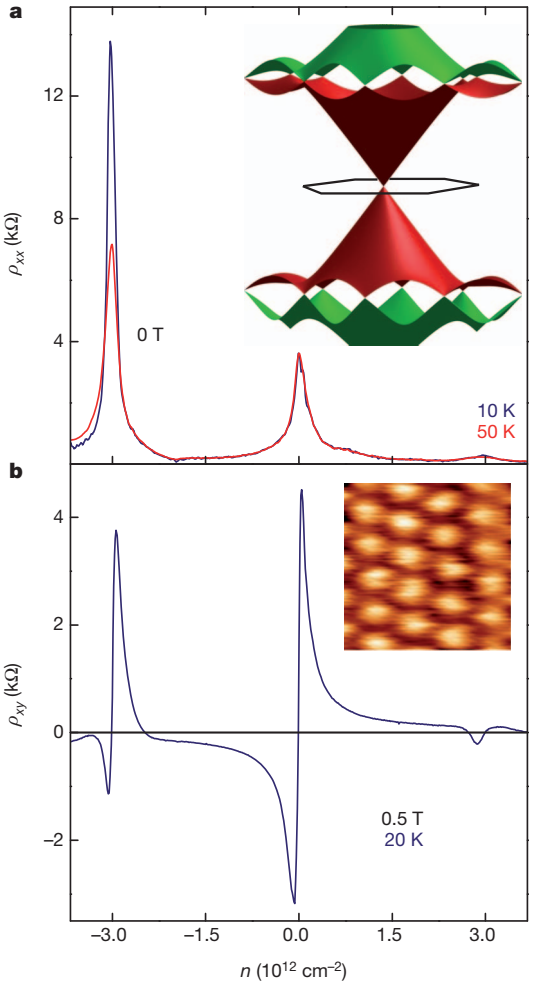

Figure 1 | Transport properties of Dirac fermions in moiré superlattices. **a**, Longitudinal resistivity, ρ_{xx}, as a function of n. Positive and negative values of n correspond to electrons and holes, respectively. The hole-side neutrality point shows a strong T dependence (Supplementary Information, section 1). Inset, one of the possible scenarios for the reconstruction of graphene's spectrum[22]. The band structure is plotted only for the first and second SBZ (shown in brown and green, respectively). Secondary Dirac cones appear in both conduction and valence bands at the edges of the SBZ, shown by the black hexagon. Where the cones merge, van Hove singularities appear in the density of states (for details, see ref. 22). **b**, The Hall resistivity, ρ_{xy}, changes sign at high electron and hole doping, revealing well-isolated secondary Dirac points. The data are for device A, for which $n_S \approx 3.0 \times 10^{12}$ cm^{-2}, yielding $D \approx 12$ nm. We fabricated 11 aligned devices, six of which had essentially the same behaviour as shown here. The only difference was in n_S, which varied between 3.0×10^{12} and 3.8×10^{12} cm^{-2} ($D \approx 11 \pm 1$ nm). One other device had $n_S \approx 7.1 \times 10^{12}$ cm^{-2}, which implies[12] that $\theta \approx 1.2°$ and required gate voltages close to dielectric breakdown. Inset, conductive atomic force microscope image of the moiré pattern for one of our devices. The centre-to-centre separation between the white spots is ~11 nm. We note that, in measurements of ρ_{xy}, both positive and negative values of B were always used to symmetrize the data and subtract a small contribution due to ρ_{xx}.

to the superlattice filling factors $\nu_S = \pm 2$, where the carrier density is counted from the hSNP. In the middle of each maximum, there is a deep minimum (narrow white stripes in Fig. 2a). The minima in ρ_{xx} are accompanied by positive and negative extrema in ρ_{xy} (Fig. 2c, d). This shows that electron-like cyclotron trajectories in graphene's valence band persist when B is quantizing (that is, when it quantizes the spectrum). With decreasing T, ρ_{xx} inside the narrow minima tends to zero and the corresponding extrema in ρ_{xy} become increasingly more pronounced, which is behaviour characteristic of the development of Shubnikov–de Haas oscillations into QHE states (Fig. 2c, d). The T dependence yields a QHE gap of ~20 meV (Supplementary Fig. 6).

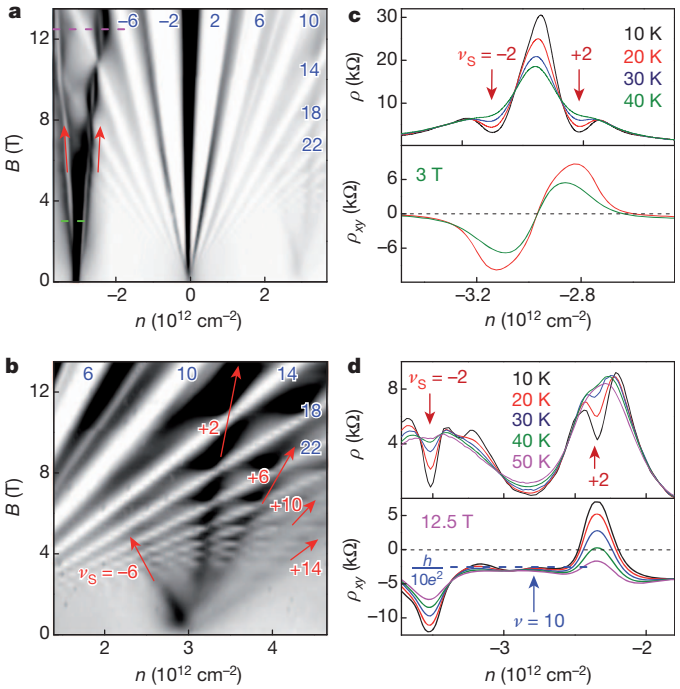

Figure 2 | Quantization in graphene superlattices. **a**, Longitudinal resistivity, $\rho_{xx}(n, B)$, at 20 K. Grey scale: white, 0 kΩ; black, 8.5 kΩ. **b**, Magnified view near the electron-side secondary neutrality point. Grey scale: white, 0 kΩ; black, 1.1 kΩ. Blue numbers denote ν for the QHE states extending from the main Dirac point. The red arrows in **a** mark the superlattice quantum states that evolve along $\nu_S = \pm 2$ (the arrows are shifted so as not to obscure the white stripes). In **b**, the red arrows indicate ν_S for the electron-side neutrality point. It is difficult to associate the electron-side superlattice Landau levels decisively with any particular value of ν_S, although the strongest peak in ρ_{xx} corresponds closely to $\nu_S = +2$. **c**, **d**, Detailed behaviour near the hSNP in fields marked by the dashed purple and green lines in **a**. Data are for device A but the same quantization behaviour was found in all devices that exhibited the secondary neutrality points. An exception is the white stripes at $\nu_S = \pm 2$, which were often smeared by inhomogeneity such that only broader maxima in ρ_{xx} remained (similar to the curves at 50 K). However, the narrow extrema in ρ_{xy}, associated with the minima in ρ_{xx} (**d**), were always present. h, Planck's constant; e, electron charge.

Unlike cyclotron gaps, this one is practically independent of B, as is seen also from the fact that the white stripes in Fig. 2a do not widen. With increasing T, the QHE states at $\nu_S = \pm 2$ gradually disappear below 50 K but the maxima in ρ_{xx} persist up to 150 K.

Another notable feature of the observed fan diagrams are the multiple peaks in ρ_{xx} accompanied by zeros or deep minima in ρ_{xy}. This is seen most clearly for devices where doping sufficiently higher than n_S can be achieved (Fig. 3). Furthermore, in all our devices near the hSNP, ρ_{xy} repeatedly changes its sign with increasing B, indicating recurrent appearance and disappearance of electron-like orbits within graphene's valence band (Fig. 3b, e and Supplementary Figs 4 and 5). This means that, for a given n, the magnetic field alone can repeatedly generate new neutrality points. Such 'third-generation' neutrality points occur periodically as n and $1/B$ vary, and form distinct groups characterized by particular values of $1/B$ (Fig. 3 and Supplementary Information, section 3). Their periodicity in $1/B$ is accurately described by unit fractions, ϕ_0/q, of the magnetic flux, $\Phi = BS_{\otimes}$, per superlattice unit cell area, $S_{\otimes}$, where q is integer. In the conduction band, the fan diagrams also exhibit Landau levels extending from the secondary Dirac point, and numerous third-generation neutrality points with the same $1/B$ periodicity are visible in Figs 2b and 3a, b. These features are weaker than those in the valence band. For example, the resistivity peak at the electron-side neutrality point is no longer there for $B \approx 1$ T (Fig. 2b) and we did not observe the secondary QHE in the conduction band.

The observed superlattice behaviour suggests that complex spectral changes are induced by quantizing B. Theoretically, the problem is

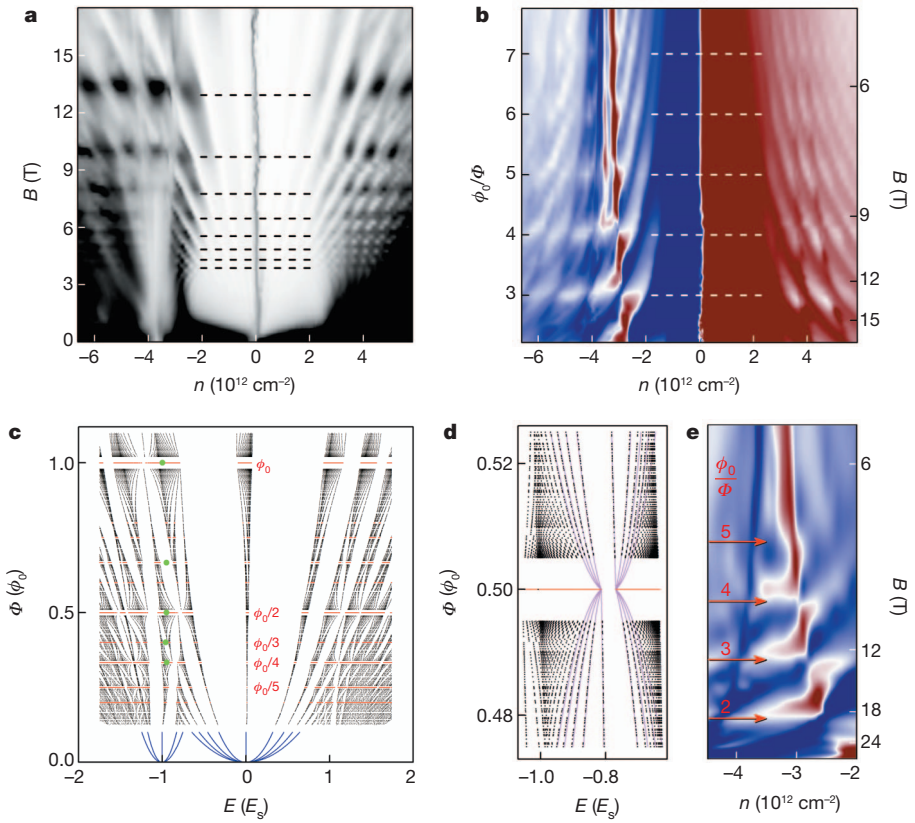

Figure 3 | Zak-type cloning of third-generation Dirac points. **a**, Longitudinal conductivity, $\sigma_{xx} = \rho_{xx}/(\rho_{xx}^2 + \rho_{xy}^2)$, as a function of n and B (device B). Grey scale: white, 0 kΩ; black, 2.2 mS. The dashed lines indicate $B_q = (1/q)\phi_0/S_\otimes$ with $q = 3$–10, where $S_\otimes$ is determined from the measured $n_S \approx 3.8 \times 10^{12}\,\mathrm{cm}^{-2}$ as $S_\otimes = 4/n_S$, which corresponds to the complete filling of the first SBZ[22]. **b**, Hall resistivity, ρ_{xy}, for the same device as a function of n and $1/B$ (the latter expressed as ϕ_0/Φ on the left axis). The dashed white lines show the periodicity of Zak oscillations. Colour scale: navy, −2 kΩ; white, 0 kΩ; wine, 2 kΩ. In both plots, $T = 2$ K. **c**, Hofstadter-like butterfly for the graphene-on-hBN superlattice. The electronic states are calculated following the approach in ref. 24 and are shown by black dots. For simple fractions p/q, we plot energies of the states in red. The regions around $\Phi = \phi_0 p/q$ are empty because the corresponding supercells are too large for us to do the necessary calculations[22,24]. The blue curves show several low Landau levels for small B, which were calculated analytically for main and secondary Dirac fermions with parameters of the zero-B spectrum. The green dots indicate the position of the Fermi level for $n = -n_S$ (Supplementary Information). **d**, Section of **c** with superimposed Landau levels calculated as functions of δB (magenta). **e**, Hall resistivity, $\rho_{xy}(n, 1/B)$, for device C ($n_S \approx 3.6 \times 10^{12}\,\mathrm{cm}^{-2}$) measured up to 29 T. The left and right axes are as in **b**. The same oscillatory behaviour is found for all our devices and is seen most clearly near the hSNP, where new neutrality points appear periodically for $\phi_0/\Phi = q$, as shown by the arrows. Colour scale: navy, −3 kΩ; white, 0 kΩ; wine, 3 kΩ. $T = 20$ K. Full plots of $\rho_{xy}(n, B)$ for devices B and C are provided in Supplementary Information, section 3.

somewhat similar to that originally discussed by Zak[23] and Hofstadter[9] and later considered for two-dimensional electron systems[3] in semiconductor superlattices and for Dirac fermions in twisted bilayers[24]. The most general, but not proven, prediction is that superlattice spectra should be 'self-similar'; that is, they should consist of multiple clones of an original spectrum, which appear at values of B such that $\Phi = \phi_0(p/q)$, where both p and q are integer. Our case of graphene on hBN is analysed in Supplementary Information, and the main theoretical results are summarized in Fig. 3c, d.

Figure 3c shows that the superlattice potential results in additional structure within each Landau level, which effectively broadens them with increasing B. The structured Landau levels extending from the main and secondary Dirac points strongly mix at high doping, $|E| \geq E_S = \hbar v_F(\pi n_S)^{1/2}$. The resulting pattern is different from that in semiconductor superlattices with a parabolic spectrum and weak modulation[3,7,8]. In the latter case, the fractal structure within each Landau level can be described by the original Hofstadter butterfly[9], which appears periodically as a function of ϕ_0/Φ. In our case, in which there is a Dirac-like spectrum and strong modulation, the fractal pattern depends on the Landau level index, N, and B (Supplementary Information, section 5).

The calculated spectrum allows us to understand many features observed experimentally. Indeed, Fig. 3c shows a self-similarity such that magnetic states tend to entwine at $\Phi = \phi_0 p/q$, forming the fractal structure of the pattern. The strongest entwining occurs for unit fractions (that is, $p = 1$), and this results in an overall periodicity in $1/B$ with a period of $S_\otimes/\phi_0$, in agreement with the experiment (Fig. 3a, b). The periodicity can be traced to the fact that for $\Phi = \phi_0/q$ the system can be considered a new superlattice that has a unit cell q times larger than the original and that is placed in zero effective magnetic field[23]. An example of the resulting magneto-electronic (Zak) bands[23] is given in Supplementary Fig. 8.

We find that in our case Zak bands feature slightly gapped Dirac spectra. This finding is illustrated in Fig. 3d, which, as an example, magnifies a part of Fig. 3c near the hSNP and $\Phi = \phi_0/2$. Using the Zak spectrum calculated for $\Phi = \phi_0/2$, we can obtain its Landau quantization in small reduced fields, $\delta B = B - B_2$, where $B_2 = \phi_0/2S_\otimes$ is the zero effective field acting on the cloned Dirac spectrum. The shape of the resulting Landau levels is given by $\pm\sqrt{N|\delta B| + \Delta^2}$, where Δ is the gap in the local Dirac-like spectrum (Fig. 3d, magenta curves). Outside the empty horizontal region inaccessible in our numerical calculations (Supplementary Information, section 5), the Landau quantization of the Zak spectrum in δB yields practically the same electronic states as shown by the calculated points (Fig. 3d, black dots). Similar local Dirac spectra are found in other parts of the moiré butterfly[24] for all $B_q = \phi_0/qS_\otimes$, in agreement with the numerous third-generation neutrality points seen in the experiment. Using the calculated spectra, we have also determined the occupancy of Zak minibands for the case of four holes per moiré supercell (that is, at the hSNP) and found that for $\Phi = \phi_0/q$ the Fermi energy lies inside the

corresponding Zak minibands, whereas for $\Phi = \phi_0/(q + 1/2)$ it lies inside gaps. This explains the experimentally observed oscillations in $\sigma_{xx}(B)$.

Another experimental feature revealing Zak minibands and the hierarchy of superlattice gaps are the prominent QHE gaps at $\nu_S = \pm 2$ near the hSNP (Fig. 2). For small B, they can be considered a result of Landau quantization for secondary Dirac fermions, and their zero Landau levels become separate from the rest of the spectrum (Fig. 3c). For higher B, the resulting gaps saturate, being limited in size by the presence of van Hove singularities at the edges of the SBZ (Fig. 1a). As Zak minibands become increasingly more pronounced the secondary Landau levels intertwine with main Landau levels and, at high doping, become indistinguishable from them (Fig. 3c). Therefore, the complex pattern of Landau levels in Fig. 3 at high doping can no longer be interpreted in terms of Landau quantization of either main or secondary Dirac fermions. The pattern becomes a 'Hofstadter–Landau' butterfly, specific to our strong-modulation regime and the linear spectrum. The largest fractal gaps near the hole-side Dirac point in Fig. 3c are in agreement with the $\nu_S = \pm 2$ QHE states observed experimentally, which have activation energies almost independent of B. This behaviour is different from the case of weak modulation in semiconductor superlattices[6–8], where Landau levels become structured but do not intertwine. However, increasing B such that $\Phi > \phi_0$ can drive graphene superlattices into the regime of weak modulation (Supplementary Fig. 9). This regime is outside the range of B values available in our experiment. In addition to the large fractal gaps, our experimental data also reveal reproducible small-scale structure that cannot be traced back to either main or secondary neutrality points (see, for example, Fig. 3a, b near the hSNP at high B and Supplementary Fig. 5a). We attribute these fine features to further fractalization of the superlattice spectrum such that isolated Landau levels for the third-generation Dirac clones start being resolved (Fig. 3d). This is similar to the intra-Landau-level features reported in semiconductor superlattices[7,8] and warrants further investigation.

Graphene superlattices can be reliably fabricated for various types of transport measurement. This opens new lines of enquiry; in particular, the fractal quantization leads to such rich behaviour that its full understanding will require much further work, both theoretical and experimental. The demonstrated possibility of creating gaps at specifically chosen energies by controllably rotating graphene or other two-dimensional crystals within van der Waals heterostructures[25] can be used to design novel electronic and optoelectronic devices.

METHODS SUMMARY

Our devices were multiterminal Hall bars fabricated following the procedure described in ref. 27. In brief, monolayer graphene was deposited on top of a relatively thick (>30 nm) hBN crystal[28] and then covered with another hBN crystal. The encapsulation protects the graphene from the environment and allows high μ values, little residual doping ($<10^{11}$ cm^{-2}) and little charge inhomogeneity[27]. The interfaces between the graphene and the hBN were atomically clean over the entire active device area[25]. The whole stack was assembled on top of an oxidized Si wafer that served as a back gate. To align the crystal lattices, we used an optical microscope to choose straight edges of graphene and hBN crystallites, which indicate the principal crystallographic directions (see, for example, figure 2 of ref. 30). During the assembly, the graphene was rotated relatively to the bottom hBN crystal to make their edges parallel. We estimate our alignment precision to be $\sim 1^\circ$. The top hBN crystal was then rotated by $\sim 15^\circ$ with respect to the aligned edges, which ensured no spectral reconstruction at $E_S < 1$ eV due to the second graphene–hBN interface.

In practice, gate dielectric breakdown for oxidized silicon wafers occurs in fields less than 0.4 V nm^{-1}, and this limits achievable values of n to less than 7×10^{12} cm^{-2} ($E_S < 0.35$ eV). Accordingly, the observation of secondary Dirac points requires alignment with $\theta \leq 1^\circ$ (ref. 12). For random deposition of graphene on hBN, the probability of finding transport devices with superlattice features can be estimated to be only a few per cent, even if high gate voltages are used, which is rare given the desire to avoid accidental breakdown. Previously, we investigated more than 25 graphene-on-hBN devices[27] and none of them exhibited any sign of superlattice effects. This shows that careful alignment is essential for the observation of secondary Dirac spectra in transport measurements.

Received 4 December 2012; accepted 3 April 2013.
Published online 15 May 2013.

1. Weiss, D., Klitzing, K. V., Ploog, K. & Weimann, G. Magnetoresistance oscillations in a two-dimensional electron gas induced by a submicrometer periodic potential. *Europhys. Lett.* **8,** 179–184 (1989).
2. Weiss, D. *et al.* Electron pinball and commensurate orbits in a periodic array of scatterers. *Phys. Rev. Lett.* **66,** 2790–2793 (1991).
3. Pfannkuche, D. & Gerhardts, R. R. Theory of magnetotransport in two-dimensional electron systems subjected to weak two-dimensional superlattice potentials. *Phys. Rev. B* **46,** 12606–12626 (1992).
4. Ferry, D. K. Quantum magnetotransport in lateral surface superlattices. *Prog. Quantum Electron.* **16,** 251–317 (1992).
5. Albrecht, C. *et al.* Fermiology of two-dimensional lateral superlattices. *Phys. Rev. Lett.* **83,** 2234–2237 (1999).
6. Schlösser, T., Ensslin, K., Kotthaus, J. P. & Holland, M. Internal structure of a Landau band induced by a lateral superlattice: a glimpse of Hofstadter's butterfly. *Europhys. Lett.* **33,** 683–688 (1996).
7. Albrecht, C. *et al.* Evidence of Hofstadter's fractal energy spectrum in the quantized Hall conductance. *Phys. Rev. Lett.* **86,** 147–150 (2001).
8. Geisler, M. C. *et al.* Detection of a Landau band-coupling-induced rearrangement of the Hofstadter butterfly. *Phys. Rev. Lett.* **92,** 256801 (2004).
9. Hofstadter, D. R. Energy levels and wave functions of Bloch electrons in rational and irrational magnetic fields. *Phys. Rev. B* **14,** 2239–2249 (1976).
10. Xue, J. M. *et al.* Scanning tunnelling microscopy and spectroscopy of ultra-flat graphene on hexagonal boron nitride. *Nature Mater.* **10,** 282–285 (2011).
11. Decker, R. *et al.* Local electronic properties of graphene on a BN substrate via scanning tunneling microscopy. *Nano Lett.* **11,** 2291–2295 (2011).
12. Yankowitz, M. *et al.* Emergence of superlattice Dirac points in graphene on hexagonal boron nitride. *Nature Phys.* **8,** 382–386 (2012).
13. Park, C. H., Yang, L., Son, Y. W., Cohen, M. L. & Louie, S. G. New generation of massless Dirac fermions in graphene under external periodic potentials. *Phys. Rev. Lett.* **101,** 126804 (2008).
14. Bliokh, Y. P., Freilikher, V., Savel'ev, S. & Nori, F. Transport and localization in periodic and disordered graphene superlattices. *Phys. Rev. B* **79,** 075123 (2009).
15. Tiwari, R. P. & Stroud, D. Tunable band gap in graphene with a noncentrosymmetric superlattice potential. *Phys. Rev. B* **79,** 205435 (2009).
16. Barbier, M., Vasilopoulos, P. & Peeters, F. M. Extra Dirac points in the energy spectrum for superlattices on single-layer graphene. *Phys. Rev. B* **81,** 075438 (2010).
17. Burset, P., Yeyati, A. L., Brey, L. & Fertig, H. A. Transport in superlattices on single-layer graphene. *Phys. Rev. B* **83,** 195434 (2011).
18. Wu, S., Killi, M. & Paramekanti, A. Graphene under spatially varying external potentials: Landau levels, magnetotransport, and topological modes. *Phys. Rev. B* **85,** 195404 (2012).
19. Ortix, C., Yang, L. & van den Brink, J. Graphene on incommensurate substrates: trigonal warping and emerging Dirac cone replicas with halved group velocity. *Phys. Rev. B* **86,** 081405 (2012).
20. Zarenia, M., Leenaerts, O., Partoens, B. & Peeters, F. M. Substrate-induced chiral states in graphene. *Phys. Rev. B* **86,** 085451 (2012).
21. Kindermann, M. M., Uchoa, B. & Miller, D. L. Zero energy modes and gate-tunable gap in graphene on hexagonal boron nitride. *Phys. Rev. B* **86,** 115415 (2012).
22. Wallbank, J. R., Patel, A. A., Mucha-Kruczynski, M., Geim, A. K. & Fal'ko, V. I. Generic miniband structure of graphene on a hexagonal substrate. Preprint at http://arxiv.org/abs/1211.4711 (2012).
23. Zak, J. Magnetic translation group. *Phys. Rev.* **134,** A1602–A1606 (1964).
24. Bistritzer, R. & MacDonald, A. H. Moire butterflies. *Phys. Rev. B* **84,** 035440 (2011).
25. Haigh, S. J. *et al.* Cross-sectional imaging of individual layers and buried interfaces of graphene-based heterostructures and superlattices. *Nature Mater.* **11,** 764–767 (2012).
26. Li, G., Luican, A. & Andrei, E. Y. Scanning tunneling spectroscopy of graphene on graphite. *Phys. Rev. Lett.* **102,** 176804 (2009).
27. Mayorov, A. S. *et al.* Micrometer-scale ballistic transport in encapsulated graphene at room temperature. *Nano Lett.* **11,** 2396–2399 (2011).
28. Dean, C. R. *et al.* Boron nitride substrates for high-quality graphene electronics. *Nature Nanotechnol.* **5,** 722–726 (2010).
29. Mayorov, A. S. *et al.* How close can one approach the Dirac point in graphene experimentally? *Nano Lett.* **12,** 4629–4634 (2012).
30. Geim, A. K. & Novoselov, K. S. The rise of graphene. *Nature Mater.* **6,** 183–191 (2007).

Supplementary Information is available in the online version of the paper.

Acknowledgements We thank D. Weiss, A. MacDonald and F. Peeters for discussions. This work was supported by the European Research Council, the Körber Foundation, the Office of Naval Research, the Air Force Office of Scientific Research and the Royal Society.

Author Contributions R.V.G., L.A.P. and A.K.G. designed the project. R.V.G. and R.J. made the graphene devices. G.L.Y., D.C.E., L.A.P. and A.S.M. carried out the measurements. K.S.N., A.M., C.R.W., B.A.P., M.P. and I.V.G. provided experimental support. V.I.F., A.A.P., J.R.W., M.M.-K., A.K.G. and F.G. developed the theory. A.K.G. and V.I.F. wrote the manuscript with input from I.V.G., R.V.G., L.A.P., K.S.N. and F.G. All authors participated in discussions.

Author Information Reprints and permissions information is available at www.nature.com/reprints. The authors declare no competing financial interests. Readers are welcome to comment on the online version of the paper. Correspondence and requests for materials should be addressed to R.V.G. (blizza@gmail.com).